The Astrophysical Journal, 823:134 (9pp), 2016 June 1 doi:10.3847/0004-637X/823/2/134

THE MULTI-WAVELENGTH CHARACTERISTICS OF THE TeV BINARY LS I+61°303

L. Saha[1], V. R. Chitnis, A. Shukla[2], A. R. Rao, and B. S. Acharya
Tata Institute of Fundamental Research, Homi Bhabha Road, Colaba, Mumbai 400 005, India; labsaha@ncac.torun.pl, vchitnis@tifr.res.in
Received 2015 December 11; accepted 2016 March 24; published 2016 May 31

ABSTRACT

We study the characteristics of the TeV binary LS I+61°303 in radio, soft X-ray, hard X-ray, and gamma-ray (GeV and TeV) energies. The long-term variability characteristics are examined as a function of the phase of the binary period of 26.496 days as well as the phase of the superorbital period of 1626 days, dividing the observations into a matrix of 10 × 10 phases of these two periods. We find that the long-term variability can be described by a sine function of the superorbital period, with the phase and amplitude systematically varying with the binary period phase. We also find a definite wavelength-dependent change in this variability description. To understand the radiation mechanism, we define three states in the orbital/superorbital phase matrix and examine the wideband spectral energy distribution. The derived source parameters indicate that the emission geometry is dominated by a jet structure showing a systematic variation with the orbital/superorbital period. We suggest that LS I+61°303 is likely a microquasar with a steady jet.

Key words: gamma rays: general – radiation mechanisms: non-thermal – stars: emission-line, Be – stars: individual (LS I +61°303) – X-rays: binaries

1. INTRODUCTION

LS I+61°303, a Galactic high-mass X-ray binary system located at a distance of 2 kpc (Frail & Hjellming 1991), is detected in the energy range from radio to γ-rays exhibiting strong variable emission. It consists of a B0 main-sequence star with a circumstellar disk (i.e., a Be star) and a compact object of unknown nature. The orbital period of the system is estimated to be $P_{\rm orb} = 26.496$ days and it also exhibits long-term periodic variation with a superorbital period of $P_{\rm sup} = 1667$ days (Gregory 2002; Massi & Jaron 2013; Massi et al. 2015). However, very recently the superorbital period has been estimated to be 1626 days using 37 years of radio data (Massi & Torricelli-Ciamponi 2016). The zero orbital phase corresponds to $T_{0,\rm orb} = 2443366.775 + nP_{\rm orb}\ JD$. According to the most recent radial velocity measurements, the orbit is elliptical with an eccentricity of $e = 0.537 \pm 0.034$ and periastron passage occurring around phase $\phi = 0.275$, apastron passage at $\phi = 0.775$, superior conjunction at $\phi = 0.081$, and inferior conjunction at $\phi = 0.313$ (Aragona et al. 2009).

High angular resolution VLBI radio data has shown the presence of a high-energy particle outflow which may be related to jet-like ejection on the timescale of a orbital period (Paredes et al. 1998; Massi et al. 2004). However, the observed morphological changes in the data collected at different epochs reported by Dhawan et al. (2006) support the scenario of a binary pulsar. Recent detailed Very Long Baseline Array radio images, obtained by reprocessing the same data set, through the orbital period established the presence of one-sided and double-sided radio structures, supporting a precessing microquasar model (Massi et al. 2012).

Long-term monitoring of the source during 2007–2011 with the Proportional Counter Array (PCA) on board the *Rossi X-ray Timing Explorer* (*RXTE*) established the superorbital modulation in X-rays and a shift of the superorbital phase by 0.2 between radio and X-ray data (Chernyakova et al. 2012; Li et al. 2012). Very recently, superorbital modulation in the range of MeV–GeV γ-rays in the apastron phase (0.5–1.0) was established by the *Fermi*-Large Area Telescope (LAT; Ackermann et al. 2013) based on the data taken during the period 2008 August 4–2013 March 24.

This source has often shown complex behavior in very high-energy γ-rays. LS I+61°303 was first observed at TeV energies by the MAGIC telescope system during 2005 October–2006 March with a significance of 8.7σ in the orbital phase 0.4–0.7, establishing it as a γ-ray binary (Albert et al. 2006). The VERITAS observations carried out during 2006 September–2007 February confirmed the TeV emission from this source (Acciari et al. 2008). However, further observations of the source by both MAGIC and VERITAS have shown different flux levels (Acciari et al. 2011; Aleksic et al. 2012; Aliu et al. 2013). These observations at TeV energies show that the source behaves differently in different orbital cycles, which suggests a variable nature of the source. Variability of the source in almost all wavelengths may be related to superorbital modulation of the fluxes, which has been shown in the radio, X-ray, and MeV–GeV γ-rays detected by *Fermi*-LAT (Gregory 2002; Chernyakova et al. 2012; Li et al. 2012; Ackermann et al. 2013). Hence, the long-term multiwaveband study of this source can provide important observational support for unveiling the nature of the source and the emission mechanisms.

With this motivation, we have studied the radio, X-ray, and γ-ray data from this source collected over a period longer than the superorbital period. We have studied the variation of the flux as a function of the orbital and superorbital phases. We have also studied the multiwaveband Spectral Energy Distribution (SED) of the source in some of the phases. This paper is organized as follows. In Section 2, the data set used for these studies and the analysis procedure are described. The variation of the flux with the orbital and the superorbital phases is discussed in Section 3. The SEDs and their interpretation in terms of the microquasar model are given in Section 4, followed by a discussion and our conclusions in Section 5.

[1] Present address: Nicolaus Copernicus Astronomical Center, 87-100 Torun, Poland.
[2] Present address: Institute for Theoretical Physics and Astrophysics, Universität Würzburg, D-97074 Würzburg, Germany.

2. MULTIWAVEBAND DATA AND ANALYSIS

In the last few years, LS I+61°303 has been observed extensively by various instruments. In the present work, we have used data from the radio, X-ray, and γ-ray bands. The radio data used here are from Richards et al. (2011) and Massi et al. (2015). These are 15 GHz observations from the 40 m single-dish telescope at Owens Valley Radio Observatory (OVRO). Data on LS I+61°303 were collected during MJD 54908.8–56795.0 (2009 March–2014 May). Observations were carried out approximately twice a week.

X-ray data were obtained from PCA on board *RXTE* and the X-ray Telescope or XRT on board *Swift*. The PCA is an array of five identical Xenon-filled proportional counter units (PCUs; Bradt et al. 1993) covering an energy range from 2 to 60 keV with a total collecting area of 6500 cm^2. Data were collected over the period MJD 50143–55924 and a standard analysis procedure was used to generate PCA light curves over the energy range of 2–9 keV.

The XRT on board *Swift* consists of a grazing incidence Wolter I telescope which focuses X-rays on a CCD (Burrows et al. 2005). This instrument has an effective area of 110 cm^2, a 23.6 arcmin field of view (FOV), and 15 arcsec resolution (half-power diameter). It covers an energy range of 0.2–10 keV. *Swift*-XRT light curves were obtained from the *Swift* website.[3] Data were collected over the period MJD 53980–57039 (2006 September 2–2015 January 17). The details of the procedure used for generating these light curves are given in Evans et al. (2007).

High-energy γ-ray data are obtained from LAT on board *Fermi*. *Fermi*-LAT is a pair production telescope (Atwood et al. 2009) covering an energy range of 20 MeV–300 GeV with a FOV of $\geqslant$2.5 sr. The data taken over the period MJD 54682.9–57145.9 (2008 August 4–2015 May 3) were analyzed in the present work. A circular region of interest (ROI) with a radius of 15° centered at the position of R.A.(J2000) = $02^h\ 40^m\ 34^s$ and decl.(J2000) = 61° 15′ 25″ was used for extracting the data. *Fermi* Science Tools (FST-v10r0p5) with event class Pass 8 data were used for Galactic point source analysis. Since the Earth's limb is a strong source of background γ-rays, they were filtered out with a zenith-angle cut of 100°. A python-based software tool *enrico* (Sanchez & Deil 2013) was used to perform standard binned likelihood analysis. The γ-ray events in the data were binned in 8 logarithmic bins in energies between 300 MeV and 300 GeV. Since the point-spread function of LAT is large, the sources from outside of the ROI may contribute at low energies, affecting true estimates of the fluxes for the sources considered in this analysis. In order to account for this, the exposure map was expanded by another 10° outside the ROI, for all of the events, as suggested by Abdo et al. (2009).

We studied the spectral properties of the γ-ray emission by comparing the observational results with the models of the sources present in the ROI. To obtain the best-fit model parameters, the spatial distribution and spectral models of the sources are convolved with the instrument response function (IRF) and the exposure of the observation. In this work, we used the newly introduced IRF version *P8R2_SOURCE_V6*. There are 85 point-like sources and some diffuse background sources from the third *Fermi*-LAT catalog located in the ROI. In order to account for the emission from background sources, we considered a two-component background model: a diffuse Galactic emission (gll_iem_v06.fits) component and an isotropic emission component (iso_P8R2_SOURCE_V6_v06.txt) consisting of emission from extra galactic background, unresolved sources, and instrumental background.

The binned likelihood analysis was used for both background and source modeling using the *gtlike* tool of FST. The spectral parameters for the source outside the 3° region centered at the LS I+61°303 position were kept fixed. However, except for the normalization for the point-like background sources, the parameters were fixed or varied based on their strength and distance from the center of the ROI. The light curve was generated over the energy range 300 MeV–300 GeV.

For the VHE or TeV band, published data collected during 2005–2011 from MAGIC (Albert et al. 2009) and VERITAS (Acciari et al. 2008, 2011; Aliu et al. 2013) experiments are used. These are the ground-based atmospheric Cherenkov experiments located in La Plama and Arizona, respectively.

3. MULTIWAVEBAND FLUX VARIATION

In order to study the variation of flux as a function of the orbital and superorbital phases, data sets from various wavebands were folded in 10 superorbital phase bins using the ephemeris given by Massi & Torricelli-Ciamponi (2016). Each bin corresponds to 163 days. Furthermore, in each phase bin, 10 orbital phase bins were generated. The average flux was estimated in each of these 10 × 10 phase bins. X-ray fluxes from *Swift*-XRT and *RXTE*-PCA in 10 × 10 orbital versus superorbital bins are shown in the top left and the top right panels of Figure 1, respectively. These panels show a definite pattern in the variation of flux over the orbital and superorbital phases for both XRT and PCA data. It can be seen from the figure that the source is bright in the orbital phase range ∼0.4–0.8, while the corresponding superorbital phase is at ∼0.3–0.8. The highest flux in each of the orbital cycles shifts toward apastron passage as the superorbital phase value increases. Similar plots generated for the γ-ray data from *Fermi*-LAT and 15 GHz radio data from OVRO are given in the middle panels of Figure 1. As noted by earlier studies, there is a definite shift in the pattern for the radio data: the maximum flux is at the same orbital phase range (0.4–0.8) as in the X-ray data, but the superorbital phase range is shifted to 0.7–1.4. The *Fermi*-LAT data shows some indication of enhanced emission in the orbital phase 0.4–0.8, but unlike the other wavebands, the enhancements in the superorbital phases are not very clear. The plots for the VHE γ-ray data from VERITAS and MAGIC are shown in the bottom panels of Figure 1. However, the data set is not extensive enough to detect any trend in this case.

To investigate this aspect further, variation of the flux as a function of superorbital phase was studied in various orbital phase bins. Variation of the X-ray count rates from the *Swift*-XRT with superorbital phase is shown in the top left panel of Figure 2. Similar plots for *RXTE*-PCA, *Fermi*-LAT, and OVRO are shown in the top right, bottom left, and bottom right panels of the same figure, respectively. In each panel, different curves from the bottom to top correspond to orbital phases 0–0.1, 0.1–0.2, ..., 0.9–1.0. Curves are shifted with respect to each other for the sake of clarity. Error bars correspond to the standard deviation in each bin. To parameterize this variation, data are fit with a constant and alternatively with a sine function of the form $f(t) = f_o + A \times \sin(\phi_s - \phi_o)$, where f_o, A, and ϕ_o are model parameters and ϕ_s is the superorbital phase. The sine function

[3] http://www.swift.ac.uk/user_objects/

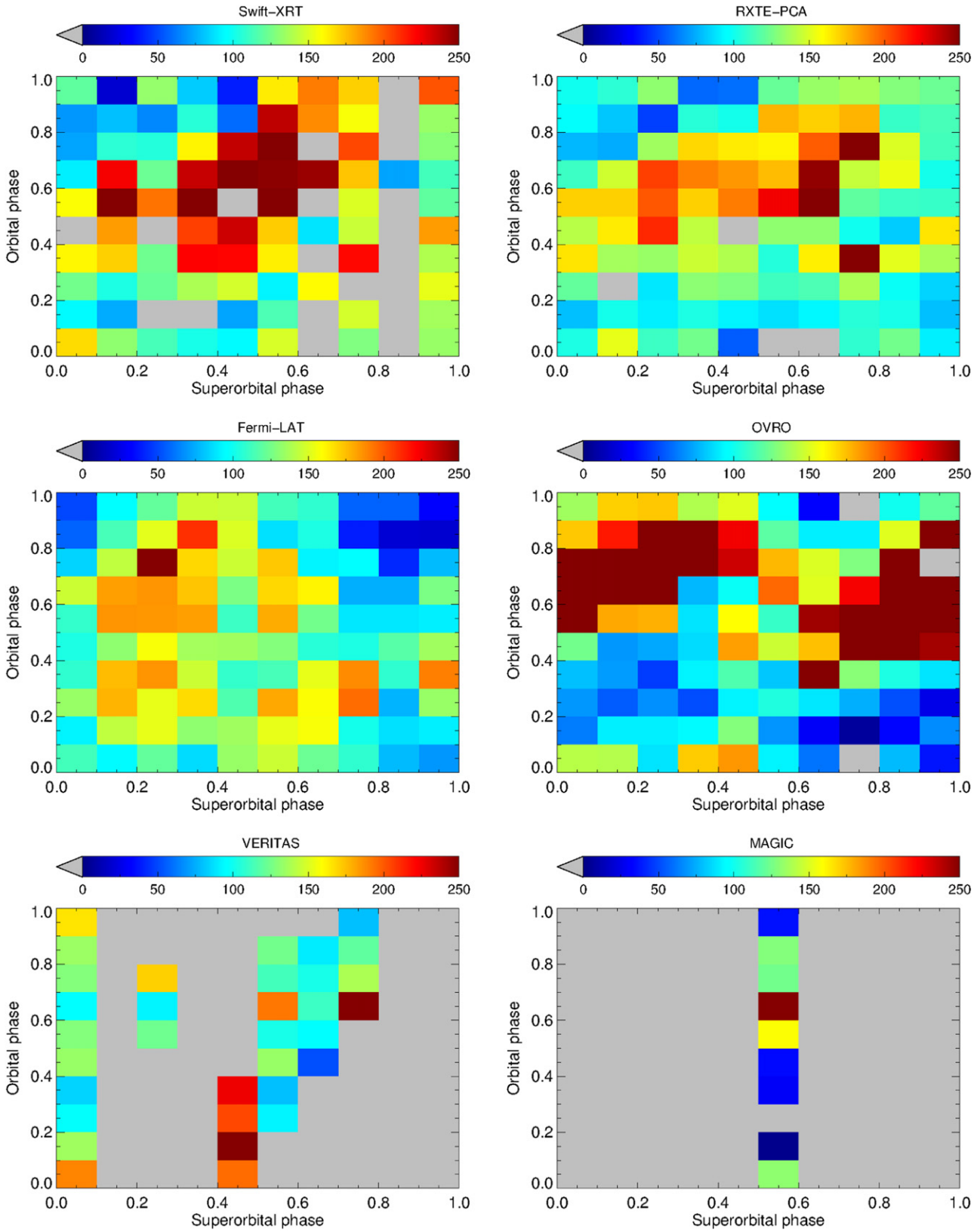

Figure 1. Multiwaveband flux as a function of orbital and superorbital phases. Top panels show X-ray flux from XRT data in the left panel and PCA data in the right panel. Middle left panel corresponds to γ-ray data from *Fermi*-LAT and middle right panel shows radio data from OVRO. Bottom panels correspond to VHE γ-ray flux from VERITAS (left panel) and MAGIC (right panel). Flux values in each panel are normalized setting median flux to 125, i.e., the middle of the scale.

with a period of 1626 days gives a better fit than the constant. It can be seen from the figure that there is a definite shift in the superorbital phase for the peak flux with respect to the orbital phase. Phase at the peak of the function, peak function value, and the ratio of the maximum to the minimum function values are listed in Table 1. Results are only given for those cases where

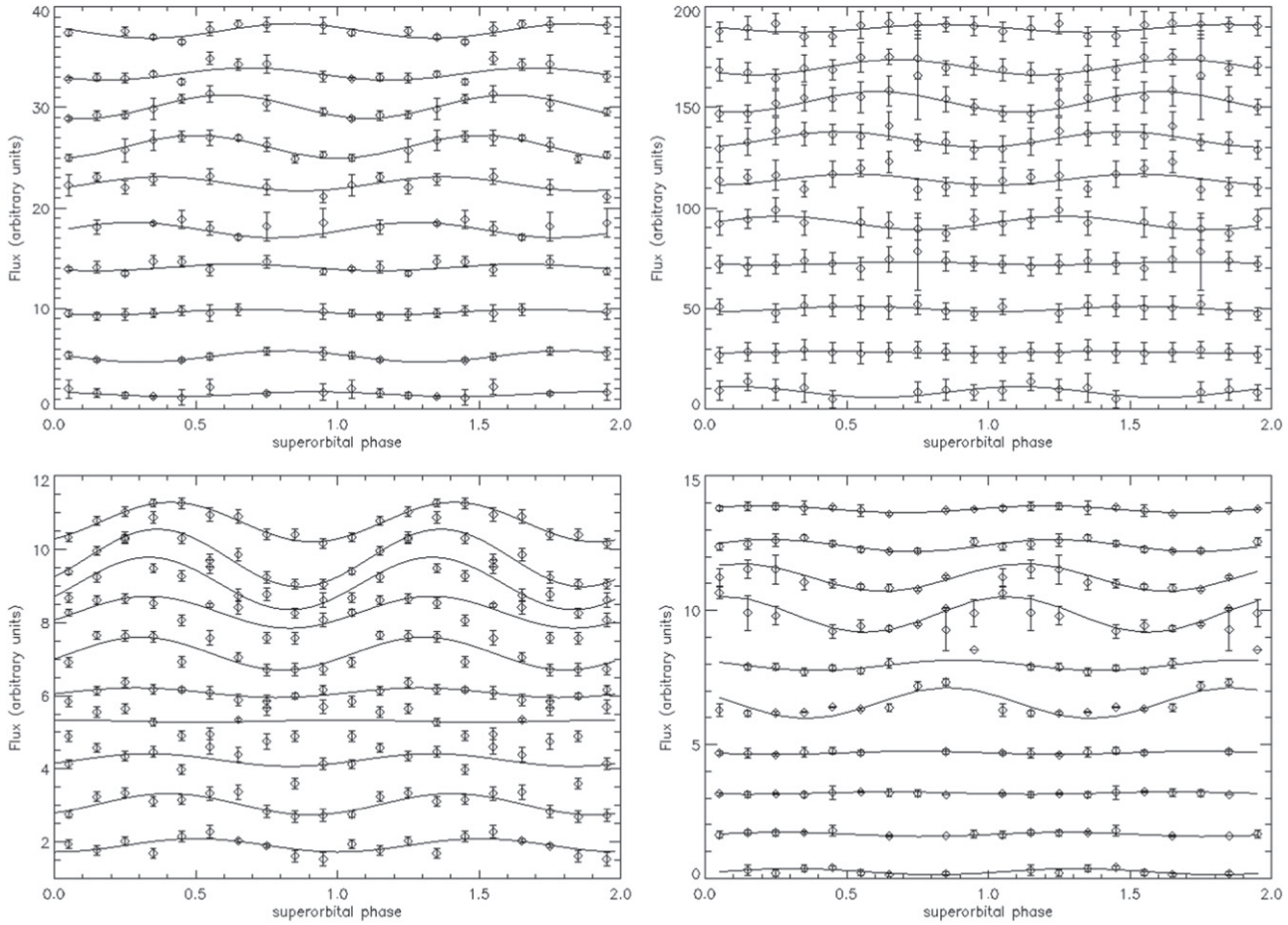

Figure 2. Variation of flux with superorbital phase for XRT (top left), PCA (top right), *Fermi*-LAT (bottom left), and OVRO (bottom right). In each panel, the curves from bottom to top correspond to orbital phases 0–0.1, 0.1–0.2, ..., 0.9–1.0. These curves are shifted along the *Y*-axis for the sake of clarity.

Table 1
Peak Flux and Corresponding Superorbital (SO) Phase from Sine Function Fit in Various Orbital Phase Bins

Orbital Phase	XRT			PCA			*Fermi*-LAT			OVRO		
	SO Phase at Peak	Peak Flux (10^{-1} counts s^{-1})	Ratio (max /min)	SO Phase at Peak	Peak Flux (counts s^{-1})	Ratio (max /min)	SO Phase at Peak	Peak Flux (10^{-7} ph cm^{-2} s^{-1})	Ratio (max /min)	SO Phase at Peak	Peak Flux (10^{-2} Jansky)	Ratio (max /min)
0.0–0.1	...	...	...	...	...	...	...	...	...	0.30	4.19	23.88
0.1–0.2	...	...	...	...	...	...	...	...	...	0.26	2.22	3.25
0.2–0.3	...	...	...	...	...	...	...	...	...	0.58	2.32	1.86
0.3–0.4	...	...	...	...	...	...	...	...	...	0.70	2.51	2.01
0.4–0.5	0.28	2.79	3.16	0.26	1.60	1.80	0.28	2.21	1.13	0.80	8.73	7.75
0.5–0.6	0.38	3.12	1.86	0.54	1.83	1.68	0.30	2.60	1.53	0.90	6.50	2.58
0.6–0.7	0.50	3.26	3.55	0.46	1.75	1.70	0.34	2.71	1.47	0.06	9.31	3.10
0.7–0.8	0.60	3.27	3.79	0.62	1.64	2.12	0.34	2.78	2.06	0.10	9.93	2.85
0.8–0.9	0.60	2.53	3.19	0.66	1.46	2.50	0.36	2.54	2.60	0.30	6.41	6.91
0.9–1.0	0.84	2.34	2.71	0.78	1.16	1.51	0.42	2.28	1.89	0.26	3.82	1.82

modulation is seen clearly in Figure 2. Figure 3 shows these results graphically where the superorbital phase for the peak of the function value is plotted as a function of the orbital phase bins for XRT, PCA, *Fermi*-LAT, and OVRO data. This figure clearly shows the trend of increasing superorbital phase for the peak as a function of orbital phase near apastron. The wavelength-dependent phase difference between superorbital phase for a given orbital phase bin is also evident. This difference remains more or less constant in various orbital phase bins near apastron.

4. SPECTRAL ENERGY DISTRIBUTION

We have investigated the spectral properties of the source at different orbital and superorbital phases. Following Figure 1, three different regions were chosen. Two of the regions are bright in most of the wavebands and the third one is of low brightness. These regions are (i) the Superorbital phase: 0.3–0.5, the Orbital phase: 0.6–0.8; (ii) the Superorbital phase: 0.5–0.7, the Orbital phase: 0.6–0.8; and (iii) the Superorbital phase: 0.0–0.2, Orbital phase: 0.0–0.2 (hereafter state1, state2, and state3, respectively). X-ray and *Fermi*-LAT spectral data

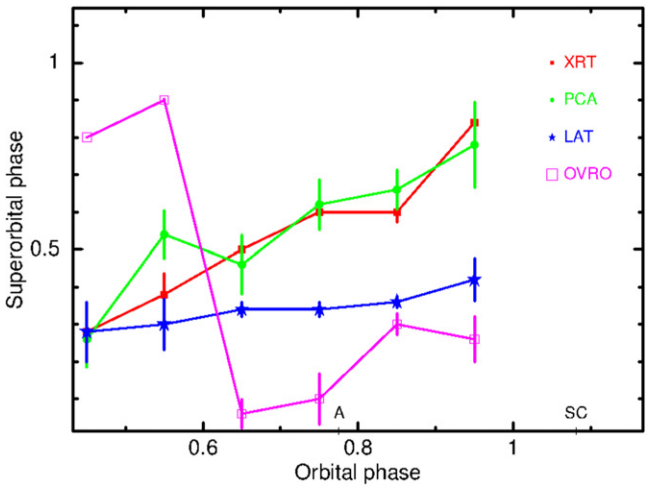

Figure 3. Superorbital phase at peak flux from the fitted sinusoidal function given in Table 1 as a function of orbital phase bins for XRT, PCA, *Fermi*-LAT, and OVRO data. Positions for apastron (A) and superior conjunction (SC) are marked.

were analyzed for these three regions. The *Fermi*-LAT analysis procedure has already been described in Section 2. We have analyzed the spectral data from *Swift*-XRT and *RXTE*-PCA corresponding to the states mentioned above. Some details of these observations are given in Table 2. Dates for XRT and PCA observations for each of the three states are listed in the table along with the total observation duration.

In the case of XRT, we have fit the spectrum over the energy range of 0.3–10 keV. Source and background photons were selected using the tool XSELECT. Data were recorded in Photon Counting (PC) mode for these observations. Source photons were selected from a circular region with a radius of 20 pixels (i.e., 47 arcsec), whereas a nearby circular region with a radius of 40 pixels was used for extracting background photons. Events with grades 0–12 were selected in this analysis. The spectral data were rebinned using the tool GRPPHA with 20 photons per bin. Standard response matrices and ancillary response files were used.

In the case of PCA, standard 2 data with a time resolution of 16 s and 128 channels of energy information were used. Data were analyzed using HEASOFT (version 6.15). For each observation, data were filtered using the standard procedure given in the *RXTE* Cook Book. The tool "pcabackest" was used for the generation of the background model, and calibration files for "faint" source (less than 40 ct/s/PCU) from *RXTE* GOF were used. To improve the statistics, only data from the top layer of PCU2 were used.

A combined spectral fit was performed for XRT and PCA data. The PCA spectrum was normalized with the XRT spectrum for this purpose. The XRT and PCA spectra covering the energy range 0.7–20 keV were fit using XSPEC with a power law with line-of-sight absorption, which was kept free during the fit. Model parameters for the combined fit as well as for only XRT data are listed in Table 3. Since the bandwidth of the data is quite limited, we find a correlation between the power-law index and absorption, indicating that a steeper power law is compensated for by large absorption. For the wideband fitting, we use the joint XRT–PCA fit because the higher-energy data from PCA better constrains the power law.

Fermi-LAT SEDs for the three states fit with a cutoff power law are given in Figure 4 and model parameters are listed in Table 4. Some differences can be seen in the spectral indices for γ-rays between state1 and other states (see Table 4). In the case of X-ray data, some steepening of the spectrum is seen as the flux decreases, as indicated by the variation in the spectral index (see Table 3).

We have investigated the spectral energy distributions (SEDs) of the source. The state3 does not have TeV data, and hence we have conducted a detailed SED study of the other two states. These states are bright in all wavebands, and hence can be used as a template to understand the emission mechanisms. VERITAS spectral data obtained from Acciari et al. (2011) corresponds to state1. For the radio flux, the average of 15 GHz data from OVRO described in Section 2 is used. This sets an upper limit on the modeled radio flux. In addition, we have also plotted radio data from Strickman et al. (1998), which correspond to an orbital phase of 0.8 and a superorbital phase of 0.8.

Since LS I+61°303 is identified as a potential microquasar based on radio observations, high-energy emission is likely to be produced in jets. In the case of microquasars, the compact object could be a neutron star or a black hole accreting matter from a companion star, which presumably drives a relativistic outflow or jet from the compact object. The acceleration of charged particles in the jet produces high-energy emission. We have considered this scenario for modeling the SEDs. In the context of a leptonic model, the low-energy emission arises from Synchrotron emission from ultra-relativistic electrons in the jet. On the other hand, the high-energy emission arises from inverse Compton scattering of soft photons, which could be either soft photons from Synchrotron radiation (Synchrotron Self-Compton or SSC model) or photons from a companion star or accretion disk (External Compton model). In this work, a relativistic jet making an angle of 30° (Gupta & Bottcher 2006 and reference therein) with our line of sight is considered. Electrons are assumed to have a broken power-law energy spectrum given by

$$\frac{dn_e}{d\gamma} \propto \begin{cases} \gamma^{-\alpha} \text{ for } \gamma < \gamma_{br} \\ \gamma^{-\beta} \exp\left(-\dfrac{\gamma}{\gamma_c}\right) \text{ for } \gamma_{br} \leqslant \gamma \leqslant \gamma_c, \end{cases}$$

where n_e denotes the number density of the electrons, γ is the Lorentz factor of the electron, α and β are spectral indices, γ_{br} is the break energy, and γ_c is the highest energy of the electron.

For this source, the distance is taken to be 2 kpc (Hutchings & Crampton 1981; Frail & Hjellming 1991) and the Lorentz factor for bulk motion is assumed to be 1.25 (Massi et al. 2004). The models are shown for state1 and state2, respectively, in Figures 5 and 6.

Here, it is assumed that the radio, X-ray, and γ-ray emission originate in the same region and that the magnetic field in the emission blob is quite high, of the order of 10^3 G. The rest of the model parameters are fit and these parameters are listed in Table 5. To explain the TeV γ-ray emission, it was necessary to include the IC of photons from the accretion disk or companion star in addition to the SSC component. The radiation density ($U_{\rm rad}$) is estimated from the luminosity L using the expression $U_{\rm rad} = L/4\pi R^2 c$, where R is the distance of the emission volume from the companion star or the accretion disk. The radiation density from the companion star, with $L_c = 2 \times 10^{38}$ erg s^{-1} and a distance of $R \sim 10^{12}$ cm, is about 4 orders of magnitude higher than the corresponding radiation density from the accretion disk.

Table 2
Observation Log for XRT and PCA

State	Instrument	Observation Dates	Number of Observations	Total Duration Seconds
1	XRT	2010 Oct 22, 2010 Nov 18, 2010 Dec 17, 2014 Oct 18,	13	15805
Superorb. phase : 0.3–0.5		2014 Oct 20–2014 Oct 23, 2014 Nov 14, 2014 Nov 15,		
Orbital phase : 0.6–0.8		2014 Dec 11–2014 Dec 13		
	PCA	2010 Feb 25, 2010 Feb 28, 2010 Mar 24, 2010 Mar 28,	18	22416
		2010 Apr 20, 2010 Apr 22, 2010 May 16, 2010 May 18,		
		2010 Jun 14, 2010 Jul 10, 2010 Aug 05, 2010 Sep 02,		
		2010 Sep 26, 2010 Sep 30, 2010 Oct 25, 2010 Nov 17,		
		2010 Nov 21, 2010 Dec 16		
2	XRT	2006 Sep 05, 2006 Nov 21–2006 Nov 24, 2006 Dec 18,	10	20147
Superorb. phase : 0.5–0.7		2006 Dec 20, 2006 Dec 22, 2011 Jan 14, 2011 Oct 01		
Orbital phase : 0.6–0.8	PCA	2006 Oct 27, 2006 Oct 29, 2011 Jan 09, 2011 Jan 13,	20	24384
		2011 Feb 06, 2011 Feb 09, 2011 Mar 06, 2011 Mar 31,		
		2011 Apr 03, 2011 Apr 28, 2011 May 22, 2011 May 26,		
		2011 Jun 19, 2011 Jul 13, 2011 Jul 17, 2011 Aug 10,		
		2011 Aug 14, 2011 Sep 07, 2011 Oct 03, 2011 Oct 30		
3	XRT	2008 Oct 22, 2008 Nov 19, 2008 Dec 17, 2013 Nov 23,	6	10266
Superorb. phase : 0.0–0.2		2013 Dec 14, 2014 Jan 11		
Orbital phase : 0.0–0.2	PCA	2008 Oct 22, 2008 Oct 25, 2008 Nov 17, 2008 Nov 19,	21	32912
		2008 Dec 13, 2008 Dec 17, 2009 Jan 10, 2009 Feb 04,		
		2009 Feb 07, 2009 Mar 05, 2009 Mar 29, 2009 Apr 02,		
		2009 Apr 26, 2009 May 21, 2009 May 25, 2009 Jun 18,		
		2009 Jul 12, 2009 Jul 15, 2009 Aug 08		

Table 3
Best-fit Parameters of a Power-law (with Absorption) Fit to the Data for XRT and PCA

	Only XRT		
	N_H (10^{22} cm^{-2})	Alpha	Norm
state1	0.68 ± 0.05	1.58 ± 0.06	$(2.51 \pm 0.21) \times 10^{-3}$
state2	0.70 ± 0.05	1.53 ± 0.05	$(3.08 \pm 0.20) \times 10^{-3}$
state3	0.69 ± 0.11	1.47 ± 0.12	$(1.25 \pm 0.20) \times 10^{-3}$
	XRT+PCA (All Layers)		
	N_H (10^{22} cm^{-2})	Alpha	Norm
state1	0.81 ± 0.04	1.79 ± 0.03	$(3.22 \pm 0.15) \times 10^{-3}$
state2	0.90 ± 0.03	1.78 ± 0.03	$(4.27 \pm 0.17) \times 10^{-3}$
state3	1.05 ± 0.08	1.95 ± 0.05	$(2.25 \pm 0.18) \times 10^{-3}$

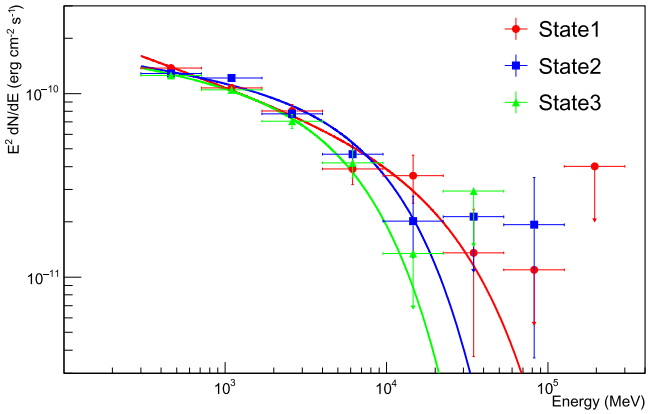

Figure 4. Cutoff power-law fit to *Fermi*-LAT data for the three different states. Best-fit curves are shown as solid lines.

Table 4
Parameters of a Cutoff Power-law Fit to the *Fermi*-LAT Data for Three Different States

Parameters	state1	state2	state3
α	2.31	2.12	2.12
Flux (ph cm^{-2} s^{-1})	2.48×10^{-7}	2.41×10^{-7}	2.28×10^{-7}
Ec (MeV)	30041	10000	6338
TS	2663	2727	2328

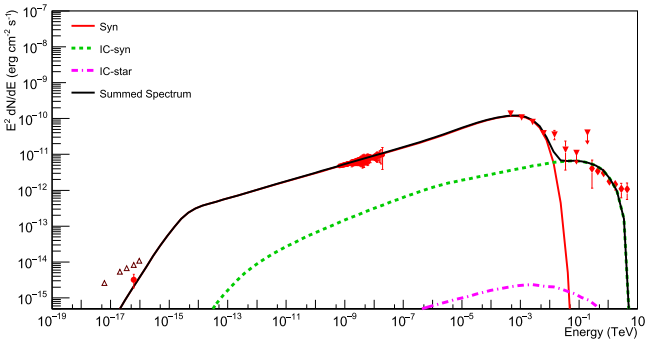

Figure 5. SED of LS I+61°303 for state1. The synchrotron and inverse Compton spectra are calculated using the parameters as given in Table 5. X-ray, *Fermi*-LAT, and VERITAS data for state1 are shown with points in red. Radio data shown in the figure do not correspond to state1. The average flux from OVRO is shown with filled red circles, whereas the radio data from Strickman et al. (1998) are shown by brown triangles.

Hence, we have considered only the seed photons from the companion star for the External Compton model. However, this spectrum cannot explain the observed data as seen from Figures 5 and 6. In this case, we have considered the radius of the

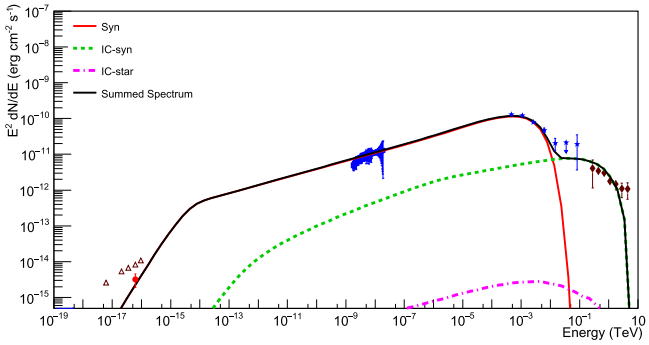

Figure 6. SED of LS I+61°303 for state2. The synchrotron and inverse Compton spectra are calculated using the same parameters as given in Table 5. X-ray and *Fermi*-LAT data for state2 are shown with blue points. Since VERITAS data for state2 are not available, state1 VERITAS data are used, which are shown in brown. Radio data are the same as in Figure 5.

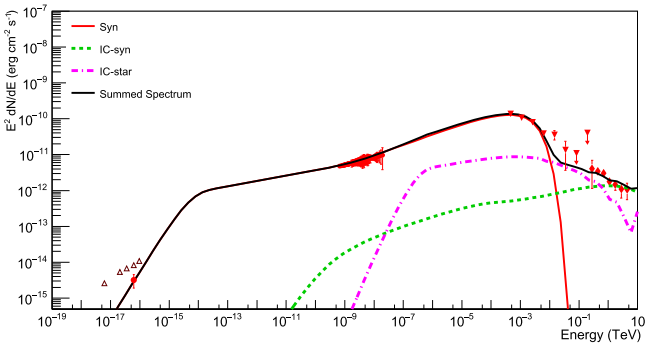

Figure 7. SED of LS I+61°303 for state1. The synchrotron and inverse Compton spectra are calculated using the same parameters given in the last column of Table 5, with the emission region radius decided from the variability timescale.

Table 5
Parameters of the Fit for the Microquasar Scenario

Parameters	state1	state2	state1 (Radius From Variability Study)
Magnetic field (Gauss)	5×10^3	5×10^3	15
$\gamma_{\rm min}$	4.4	4.9	110
$\gamma_{\rm max}$	5.6×10^6	5.4×10^6	9.0×10^7
Spectral index (α)	2.53	2.55	2.7
Spectral index (β)	2.34	2.40	2.4
Radius (cm)	11.5×10^7	18.0×10^7	7.5×10^{10}
Gamma Break	1.0×10^5	1.4×10^7	9.0×10^4
Bulk Lorentz factor	1.25	1.25	1.25
Distance (kpc)	2.0	2.0	2.0
Inclination angle(deg)	30.0	30.0	30.0
Luminosity (erg s^{-1})	3.9×10^{35}	3.8×10^{35}	4.3×10^{35}

emission volume as a parameter for the fit to the data. We can also estimate the radius of the emission volume from the variability timescale of the source. We fixed the size of the emission region according to the estimates from a variability study (Smith et al. 2009), which indicates a possible size of the emission region of $\sim 6 \times 10^{10}$ cm. Considering that the bulk Lorentz factor is 1.25, this size corresponds to $\sim 7.5 \times 10^{10}$ cm. Fixing the emission region size to this value, the model parameters were estimated and are provided in the last column of Table 5. Although the synchrotron spectrum explains the observed fluxes from radio to MeV–GeV energies, the SSC spectrum alone cannot well fit the data. Hence, we have also estimated the contribution of companion star photons for this low magnetic field case and we found that the external Compton model overestimates the observed flux at MeV–TeV energies. However, the SSC and EC models together can explain the data well if the companion star luminosity is considered to be reduced by a factor of 10. This is shown in Figure 7.

In the spectral fit, we did not consider the radio data (triangles in Figures 6–7) from VLA observations (Strickman et al. 1998), since the orbital and superorbital phases for these are different from the phases for state1 and state2. Since the energy spectrum is not available for OVRO data, we have used the average flux as an upper-limit for SED modeling, and for the chosen set of parameters the model does not overestimate the radio fluxes for the states considered above.

5. DISCUSSION AND CONCLUSIONS

Long-term timing analyses of LS I+61°303 at different wavelengths have shown some interesting characteristics for the source. The flux in various wavebands shows variation with superorbital phase and this variation is wavelength as well as binary phase dependent. At X-ray energies, as evident from Figure 1, the source is bright at orbital phases of ∼0.4−0.8 and superorbital phases of ∼0.3−0.8. Meanwhile, at radio energies, the source is bright for orbital phases of ∼0.4−0.8 and superorbital phases of ∼0.7−1.4. The γ-ray flux in the MeV–GeV band as given by *Fermi*-LAT shows a shift relative to the radio and X-ray bands. This behavior may indicate that the radio, X-ray, and γ-ray emission could originate from different regions.

The long-term superorbital modulation of the flux could support the scenario wherein the circumstellar disk of a Be star quasi-cyclically expands and shrinks (e.g., Negueruela et al. 2001). However, for such a scenario, the long-term period is variable from cycle to cycle (Rivinius et al. 2013). Recent analysis of radio data established the fact that the long-term period is quite stable over 8 cycles (Massi & Torricelli-Ciamponi 2016), which makes the scenario of quasi-cyclic variation of the circumstellar disk of the Be star for LS I+61° 303 less probable. This stable superobital modulation is attributed to periodic Doppler boosting effects of the precessional jets associated with the compact objects (Massi & Torricelli-Ciamponi 2014).

In this paper, we have seen that the modulation of flux with superorbital phase is more prominent in orbital phase bins near apastron. This can be clearly seen at various wavelengths in Figures 2 and 3. Although the long-term superorbital variation does not support the variation of circumstellar disk size, this type of superorbital modulation near the apastron could stem from the interaction of the compact object with the circumstellar disk of the Be star. The equivalent width (EW) of the Hα emission line is related to the size of the stellar disk (Zamanov & Martí 2000; Grundstrom et al. 2007). In addition, it has been found that the maximum of the EW of Hα occurs in a region around a superorbital phase of ∼0.4 (see Zamanov et al. 1999; Zamanov & Martí 2000) considering a superorbital period of 1584 days. However, if we use a superorbital period of 1626 days, then the maximum of the EW of Hα occurs at ∼0.3. From Figure 3, we see that flux of γ-rays is high at the superorbital phase of ∼0.3–0.5, which suggests that the disk plays an

important role in modulating γ-rays. Although a similar enhancement of X-rays at a superorbital phase of 0.2 is seen by Li et al. (2011) considering only peak flux, we see that the X-ray flux peaks at the superorbital phases in the range of ~0.4–0.8 depending on the orbital phase. We see that the peak radio flux is shifted further. It suggests that even if the disk size plays a significant role for γ-rays, X-ray and radio fluxes are not necessarily affected much by the size of the disk.

Figure 2 shows that for all wavebands, superorbital variability is not significant in the periastron region, whereas it is significant at apastron. This can support the scenario which assumes that the interaction between the compact object and the circumstellar disk of Be star is strong when the compact object is in the proximity of Be star. As a result, the superorbital modulation effect becomes insignificant, as suggested by Ackermann et al. (2013). However, it becomes dominant as the compact object starts moving toward the apastron region.

Another possible scenario for the modulation is related to the precession of the Be star disk about the orbital plane. If this scenario is adopted for a possible explanation of the strong superorbital modulation in the apastron phase, then the angular distance between the orbital plane and the disk plane should reach minimum. As a result, even if the compact object is far from the Be star, the smaller angular distance between the disk plane and orbital plane provides a relatively higher interaction between the compact object and the disk.

In addition to the superorbital modulation in the apastron phase (0.5–1.0), we have seen phase lag among radio, X-ray, and γ-rays. A possible explanation for the constant phase lag between the X-ray and radio is that the plasma blobs filled with high-energy particles may escape from the X-ray emission region to the radio emission region, which is at a distance ~10 times the binary separation distance, as proposed by Chernyakova et al. (2012) in the context of the pulsar wind scenario. However, in the microquasar scenario, different regions in the jets can be responsible for the phase lag. We have also seen the phase lag between radio and γ-rays. In such binary systems, γ-rays are considered to be produced by the up-scattering of radio photons or accretion disk/star photons. If the γ-rays are originating through the up-scattering of radio photons which are being produced by the same population of electrons, then there should not be any phase lag between radio and γ-rays. Hence, up-scattering of a separate population of photons could be a possible explanation for the phase lag between γ-ray and radio fluxes.

In addition to the timing analysis, we also tried to understand the spectral behavior of the source at different orbital and superorbital phases. We have chosen three different regions following flux variations for X-ray, radio, and γ-rays as function of the orbital and superorbital phase. From Figure 1, we see that the source at high energy is mostly very active in the orbital phase bin of 0.5–0.8 and the superorbital phase bin 0.3–0.7. We selected two different regions with superorbital phase 0.3–0.5, orbital phase: 0.6–0.8 (state1); superorbital phase: 0.5–0.7, orbital phase: 0.6–0.8 (state2) from this region where source is bright at all wavelengths. To compare the spectral variation with the other orbital and superorbital phases where the source is not bright, we have chosen a region with superorbital phase 0.0–0.2 and orbital phase 0.0–0.2 (state3). Based on these three different regions of orbital or superorbital phases, we have analyzed X-ray and *Fermi*-LAT data to observe the spectral behavior of the source at high energies. We found no significant differences between flux levels but we see some variations in the spectral indices at *Fermi*-LAT energies. However, we see some difference in both the spectral indices and flux levels for XRT–PCA data, although the interplay of the spectral shape and the absorption playing a role in this trend cannot be ruled out.

From the fit to the SED, we have seen that we can explain the data well considering LS I+61°303 as a microquasar. In the microquasar model, it is generally assumed that the high-energy emission comes from the region which is very close to the compact object to reduce the effect of $\gamma\gamma$ absorption due to the radiation field of the companion star (Gupta et al. 2006). The magnetic field in this region is relatively high in our model, and we have estimated an emission volume of the order of 10^8 cm. In this emission volume, some of the emitted γ-rays can be absorbed through the e^+e^- pair creation process due to X-ray photons in the emission volume. We have estimated that about 20% of γ-rays will be absorbed at TeV energies. However, larger emission volume will make this absorption insignificant. We have seen that it is possible to obtain lower values of magnetic field strength to explain the observed data in the case of a larger emission volume.

We have also seen in Section 4 that if we consider the radius of the emission volume obtained from the variability study, then the magnetic field from the model fit to the data is estimated to be ~10 G. However, we found that the SSC model alone cannot explain the TeV data well and the EC model overestimates the observed flux for the luminosity of the companion star $\sim 10^{38}$ erg s^{-1}. A lower value of this luminosity ($\sim 10^{37}$ erg s^{-1}) can well explain the data. This suggests that lower values of the magnetic field in the emission blobs are suitable for LS I+61°303 to explain the observed data constraining the luminosity of the companion star. With a high magnetic field, the Synchrotron cooling timescale is much smaller than the variability timescale, which could be as low as 2 s, as estimated by Smith et al. (2009). In our SED fitting, we have considered the emitting blob to be close to the compact object. The blob size increases as it moves away from the compact object in the jets and the magnetic field reduces. The time-averaged values of the flux from a particular region in the jet as considered by Gupta et al. (2006) could reduce the discrepancy between the Synchrotron cooling timescale and the timescale of the X-ray flux variability. From the SED, it seems that a single emission process is responsible for the X-ray and MeV–GeV data. Hence, we have considered synchrotron emission process to explain the data up to GeV energies. As a result, a high magnetic field is required to explain the data if the maximum energy of the high-energy electrons is not well above ~1 TeV. High-quality data in the hard X-ray region can establish whether a different emission component is required to explain the data in the MeV–GeV region. It can also indicate if we need a different population of electrons to explain data at different energy bands in the SED.

We have also seen that the fitted model parameters show hardening of the spectral index after the break (see Table 5). In addition, the flux levels for the different states (mainly X-ray) are different. A change in the location of the compact object relative to the companion star during the orbital and superorbital cycles and its interaction with the circumstellar disk could be responsible for the changing electron spectral distribution.

In the context of timing analysis, we have seen a phase lag among radio, X-ray, and γ-ray data which may suggest that they originate from different emission regions. However, in our present spectral modeling, we have considered a single emission zone to explain the mutiwavelength data. To support the scenario of different origins, we need simultaneous multiwavelength data for a longer period both for timing and spectral analysis. Currently, we have such observations for the radio, X-ray, and MeV–GeV gamma-rays. However, GeV–TeV data is also required to obtain a complete understanding of the source in multifrequencies.

The following major conclusions can be drawn based on the study presented here.

1. The superorbital modulation is more pronounced near the apastron for all wavelengths, supporting geometric scenarios as a cause of superorbital modulation.
2. There is a definite wavelength-dependent variation of the maximum of the superorbital flux with respect to the binary phase. This variation shows a wavelength-dependent shift.
3. Emission from radio to GeV gamma-rays during maximum emission can be modeled by a one-zone microquasar jet model. To explain the TeV emission, Comptonization from an External Compton source is necessary, especially when a low magnetic field is assumed. In this case, we suggest that the photons from the companion star, with a lower luminosity ($\sim 10^{37}$ erg s^{-1}), are adequate to explain the data.
4. Extended hard X-ray data would be necessary to constrain the synchrotron model and TeV observations across a superorbital cycle, along with X-ray measurements, would be required to make a detailed emission model for this source.

We acknowledge the use of data from the High Energy Astrophysics Science Archive Research Center (HEASARC), provided by NASA's Goddard Space Flight Center. Also the data supplied by the UK Swift Science Data Centre at the University of Leicester has been used in present work. We thank Hovatta Talvikki for providing us data from OVRO 40 m monitoring program which was used in the research by (Richards et al. 2011; supported in part by NASA grants NNX08AW31G and NNX11A043G, and NSF grants AST-0808050 and AST-1109911). We acknowledge the use of *Fermi*-LAT data and analysis tool from *Fermi* Science Support Center. We would also like to thank the MAGIC collaboration for making their published data public, which has been used in this work. We also acknowledge the VERITAS collaboration for their published data used in this work.

REFERENCES

Abdo, A. A., Ackermann, M., Ajello, M., et al. 2009, ApJS, 183, 46
Acciari, V. A., Aliu, E., Arlen, T., et al. 2011, ApJ, 738, 3
Acciari, V. A., Beilicke, M., Blaylock, G., et al. 2008, ApJ, 679, 1427
Ackermann, M., Ajello, M., Ballet, J., et al. 2013, ApJL, 773, L35
Albert, J., Aliu, E., Anderhub, H., et al. 2009, ApJ, 693, 303
Albert, J., Aliu, E., Anderhub, H., et al. 2006, Sci, 312, 1771
Aleksic, J., Alvarez, E. A., Antonelli, L. A., et al. 2012, ApJ, 746, 80
Aliu, E., Archambault, S., Behera, B., et al. 2013, ApJ, 779, 88
Aragona, C., McSwain, M. V., Grundstrom, E. D., et al. 2009, ApJ, 698, 514
Atwood, W. B., Abdo, A. A., Ackermann, M., et al. 2009, ApJ, 697, 1071
Bradt, H. V., Rothschild, R. E., & Swank, J. H. 1993, A&AS, 97, 355
Burrows, D. N., Hill, J. E., Nousek, J. A., et al. 2005, SSRv, 120, 165
Chernyakova, M., Neronov, A., Molkov, S., et al. 2012, ApJL, 747, L29
Dhawan, V., Mioduszewski, A., & Rupen, M. 2006, in Proc. VI Microquasars and Beyond: From Binaries to Galaxies, ed. T. Belloni (Trieste: PoS), 52
Evans, P. A., Beardmore, A. P., Page, K. L., et al. 2007, A&A, 469, 379
Frail, D. A., & Hjellming, R. M. 1991, AJ, 101, 2126
Gregory, P. C. 2002, ApJ, 575, 427
Grundstrom, E. D., Caballero-Nieves, S. M., Gies, D. R., et al. 2007, ApJ, 656, 431
Gupta, S., & Bottcher, M. 2006, ApJL, 650, L123
Gupta, S., Böttcher, M., & Dermer, C. D. 2006, ApJ, 644, 409
Hutchings, J. B., & Crampton, D. 1981, PASP, 93, 486
Li, J., Torres, D. F., Zhang, S., et al. 2012, ApJL, 744, L13
Li, J., Torres, D. F., Zhang, S., et al. 2011, ApJ, 733, 89
Massi, M., & Jaron, F. 2013, A&A, 554, A105
Massi, M., Jaron, F., & Hovatta, T. 2015, A&A, 575, L9
Massi, M., Ribó, M., Paredes, J. M., et al. 2004, A&A, 414, L1
Massi, M., Ros, E., & Zimmermann, L. 2012, A&A, 540, A142
Massi, M., & Torricelli-Ciamponi, G. 2014, A&A, 564, A23
Massi, M., & Torricelli-Ciamponi, G. 2016, A&A, 585, A123
Negueruela, I., Okazaki, A. T., Fabregat, J., et al. 2001, A&A, 369, 117
Paredes, J. M., Massi, M., Estalella, R., & Peracaula, M. 1998, A&A, 335, 539
Richards, J. L., Max-Moerbeck, W., Pavlidou, V., et al. 2011, ApJS, 194, 29
Rivinius, T., Carciofi, A. C., & Martayan, C. 2013, A&ARv, 21, 69
Sanchez, D. A., & Deil, C. 2013, arXiv:1307.4534
Smith, A., Kaaret, P., Holder, J., et al. 2009, ApJ, 693, 1621
Strickman, M. S., Tavani, M., Coe, M. J., et al. 1998, ApJ, 497, 419
Zamanov, R., & Martí, J. 2000, A&A, 358, L55
Zamanov, R. K., Martí, J., Paredes, J. M., et al. 1999, A&A, 351, 543